Glasslike cross-plane thermal conductivity of the kagome metals RbV_3Sb_5 and CsV_3Sb_5

Yu Pang [1,2] Jinjin Liu,[3,4] Xuanhui Fan,[5] Haobo Yang,[1] Jie Zhu [5,*] Zhiwei Wang,[3,4,6,†] Yugui Yao [3,4,6] Xin Qian [1,‡] and Ronggui Yang[1,2,§]

[1]*School of Energy and Power Engineering, Huazhong University of Science and Technology, Wuhan 430074, China*
[2]*State Key Laboratory of Coal Combustion, Huazhong University of Science and Technology, Wuhan 430074, China*
[3]*Centre for Quantum Physics, Key Laboratory of Advanced Optoelectronic Quantum Architecture and Measurement (MOE), School of Physics, Beijing Institute of Technology, Beijing 100081, China*
[4]*Beijing Key Lab of Nanophotonics and Ultrafine Optoelectronic Systems, Beijing Institute of Technology, Beijing 100081, China*
[5]*School of Energy and Power Engineering, Dalian University of Technology, Dalian 116024, China*
[6]*Material Science Center, Yangtze Delta Region Academy of Beijing Institute of Technology, Jiaxing 314011, China*

(Received 28 April 2023; revised 15 October 2023; accepted 19 October 2023; published 8 November 2023; corrected 25 September 2024)

In this paper, we report on the thermal conductivity of RbV_3Sb_5 and CsV_3Sb_5 with three-dimensional charge density wave phase transitions from 40 to 500 K measured by pump-probe thermoreflectance techniques. At room temperature, the in-plane (basal plane) thermal conductivities are found to be moderate, with 12 W m^{-1} K^{-1} of RbV_3Sb_5 and 8.8 W m^{-1} K^{-1} of CsV_3Sb_5, and ultralow cross-plane (stacking direction) thermal conductivities are observed, with 0.72 W m^{-1} K^{-1} of RbV_3Sb_5 and 0.49 W m^{-1} K^{-1} of CsV_3Sb_5. A unique glasslike temperature dependence in the cross-plane thermal conductivity is observed, which decreases monotonically even lower than the Cahill-Pohl limit as the temperature decreases below the phase transition point T_{CDW}. This temperature dependence is found to obey the hopping transport picture. In addition, a peak in cross-plane thermal conductivity is observed at T_{CDW} as a fingerprint of the modulated structural distortion along the stacking direction.

DOI: 10.1103/PhysRevB.108.205112

I. INTRODUCTION

A two-dimensional (2D) kagome lattice is a topological system with flat electronic bands, Dirac cones, and Van Hove singularities [1,2], which induce many intriguing physical phenomena such as spin-liquid states [3], bond density wave order [4], superconductivity [5], and charge density waves (CDWs) [6]. The recently discovered layered kagome metals AV_3Sb_5 (A = K, Rb, Cs) [7] with $\mathbb{Z}_2$-type nontrivial band topology [8,9] provide a unique platform for studying electron correlations, topological effects, and quantum phase transition [10,11], through various interesting phenomena, such as anomalous Hall effects [12], spontaneous symmetry breaking [13], and competition between CDWs with superconductivity [14–16].

The CDW in AV_3Sb_5 is featured by simultaneous lattice distortions both in each basal plane and the modulated stacking of different distortion patterns [17,18]. Recent measurements of magnetization, heat capacity, and electrical resistivity identify that AV_3Sb_5 undergoes a first-order CDW phase transition at the critical temperatures $T_{CDW} \approx$ 78–102 K [8,9,19]. Above the CDW transition ($T > T_{CDW}$), the crystal structure of AV_3Sb_5 consists of a high-symmetry vanadium-based kagome sublattice, as shown in Figs. 1(a) and 1(b). Lattice dynamics based on density functional theory (DFT) predicted soft acoustic phonons near the M and L points of the Brillouin zone [20], which drive the vanadium atoms in each kagome sublattice to shift away from the high-symmetry sites, forming 2 × 2 superlattices with the star of David (SD) or inverse SD (ISD) patterns [20]. DFT studies further showed that lattice distortion happens not only inside the basal planes, but such distortion is modulated with a stacking period of 2 or 4 layers [18,20]. The 2 × 2 in-plane superlattice was observed earlier using both x-ray diffraction (XRD) [8] and scanning tunneling microscopy [21–23]. The 2 × 2 × 2 superstructures have been experimentally confirmed in both KV_3Sb_5 and RbV_3Sb_5 [23,24], and CsV_3Sb_5 even shows the coexistence and competition of the 2 × 2 × 2 and the 2 × 2 × 4 superstructures that evolve with temperature [25–27]. Recent inelastic x-ray scattering and thermal diffuse scattering characterizations further suggest that the CDW phase change in AV_3Sb_5 cannot be simply interpreted as the Kohn anomaly but shows features of the order-disorder type of transition and goes beyond the weak-coupling regime [28].

Characterizing thermal properties could provide a unique angle to study the mechanisms of CDW phase transition. For example, thermal conductivity shows a peak or a sudden drop near T_{CDW}. In CDW materials with one-dimensional lattice distortions such as $K_{0.3}MoO_3$ and $(TaSe_4)_2I$ [29], a peak in temperature-dependent thermal conductivity is usually observed near the phase transition point T_{CDW} due to the excess heat carried by phasons or amplitudons as quantized modes of CDWs [30]. In layered materials such as $1T-TaS_2$ and $2H-TaSe_2$ [31,32] with 2D lattice distortions, strong electron-phonon interactions driving the phase transition are also manifested in a sudden drop in thermal conductivity

*zhujie@dlut.edu.cn
†zhiweiwang@bit.edu.cn
‡xinqian21@hust.edu.cn
§ronggui@hust.edu.cn

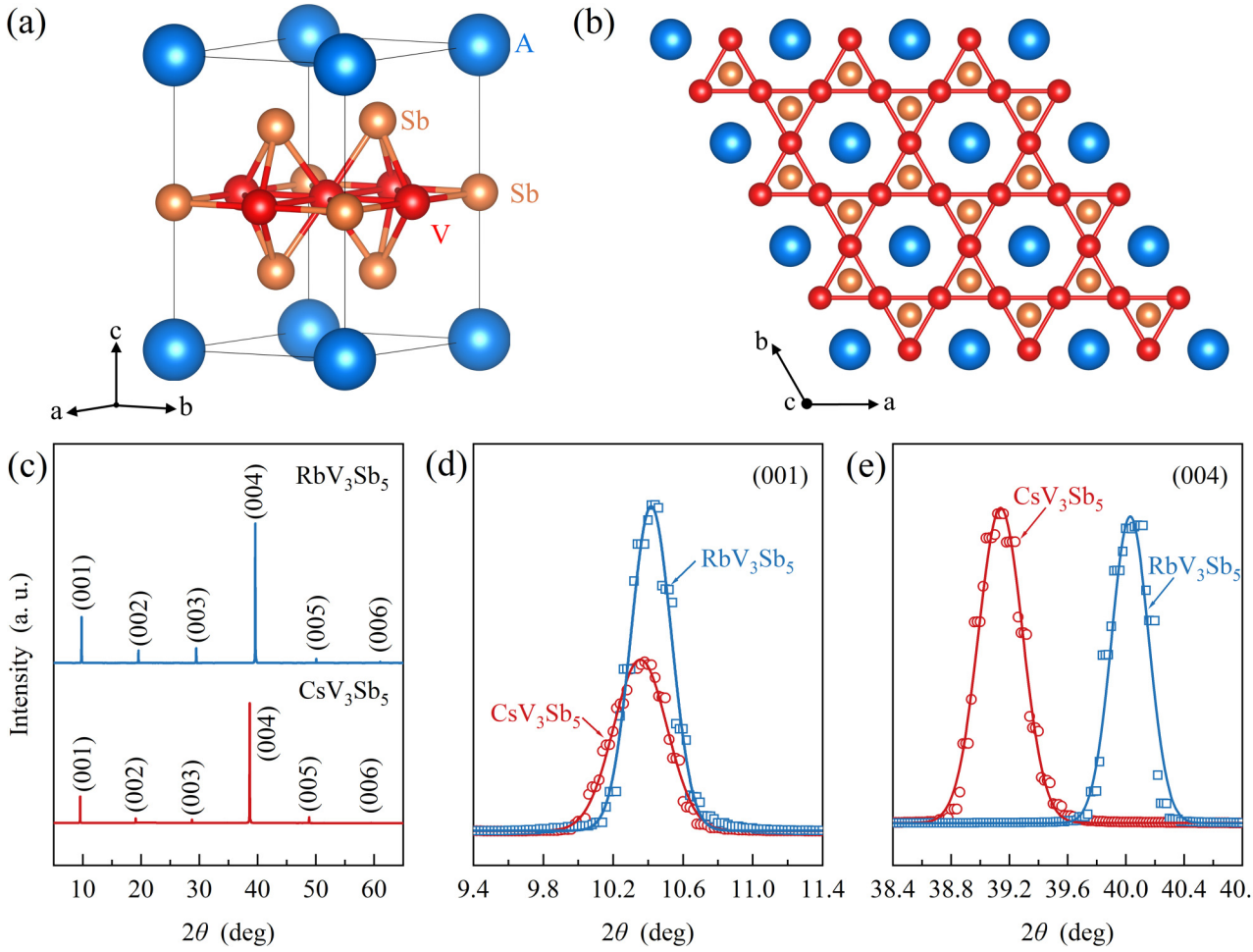

FIG. 1. (a) Unit cell of AV_3Sb_5 (A = K, Rb, Cs), (b) atomic structure of AV_3Sb_5 projected to the (001) plane. A, V, and Sb atoms are presented as blue, red, and orange balls, respectively. (c) Typical x-ray diffraction (XRD) patterns of RbV_3Sb_5 and CsV_3Sb_5 crystals. Rocking curves of RbV_3Sb_5 and CsV_3Sb_5 of (d) (001) and (e) (004) planes. Solid lines are Gaussian fitting to extract full width at half maximum (FWHM).

near T_{CDW} due to the additional scattering of heat-carrying phonons. Three-dimensional (3D) CDWs have only been identified in a few systems such as $YBa_2Cu_3O_{6.67}$ [33] and $1T-VSe_2$ [34] other than AV_3Sb_5, while how 3D lattice distortions affect thermal transport remains largely unexplored. Recently, Yang *et al.* [35] reported glasslike in-plane thermal conductivity in AV_3Sb_5 due to charge fluctuations above T_{CDW}, but measurements of cross-plane thermal conductivity near the CDW transition are still urgently needed for a complete understanding of thermal transport in layered AV_3Sb_5 with 3D CDW.

In this paper, temperature-dependent thermal conductivity along the cross-plane direction of kagome metals (RbV_3Sb_5 and CsV_3Sb_5) is measured using the pump-probe thermoreflectance technique [36–38]. We observe that RbV_3Sb_5 and CsV_3Sb_5 exhibit unique glasslike temperature dependences in the cross-plane thermal conductivity, where the thermal conductivity drops rapidly with decreasing temperatures lower than the Cahill-Pohl limit [39] at temperatures below T_{CDW}. The observed temperature dependence of cross-plane thermal conductivity is shown to obey a hoppinglike transport picture. In addition, a peak at T_{CDW} is observed in the temperature-dependent cross-plane thermal conductivity due to the structural transitions.

II. EXPERIMENTAL METHODS

A. Sample preparation and characterizations

Single crystals of RbV_3Sb_5 and CsV_3Sb_5 are prepared with binary Rb-Sb and Cs-Sb fluxes using the self-flux method [40]. Alkali metals (Rb and Cs, Alfa Aesar, 99.8%), vanadium pieces (Aladdin, 99.97%), and Sb (Alfa Aesar, 99.9999%) with a molar ratio of 9:3:17 are loaded into an alumina crucible and sealed in an evacuated quartz tube. These precursors are heated with a rate of 5 K/min and kept at 1273 K for 24 h and are then cooled to 473 K at 3 K/h. The residual flux is removed using deionized water.

XRD patterns of CsV_3Sb_5 and RbV_3Sb_5 measured using powder XRD instrumentation Bruker D8 Advance are shown in Fig. 1(c). The full width at half maximum (FWHM) of the diffraction peaks on the (00l) crystal planes of the two samples is $\sim 0.07^\circ$, indicating good crystallinity of the synthesized samples. Figures 1(d) and 1(e) shows the rocking curves of (001) and (004) planes characterized using Bruker

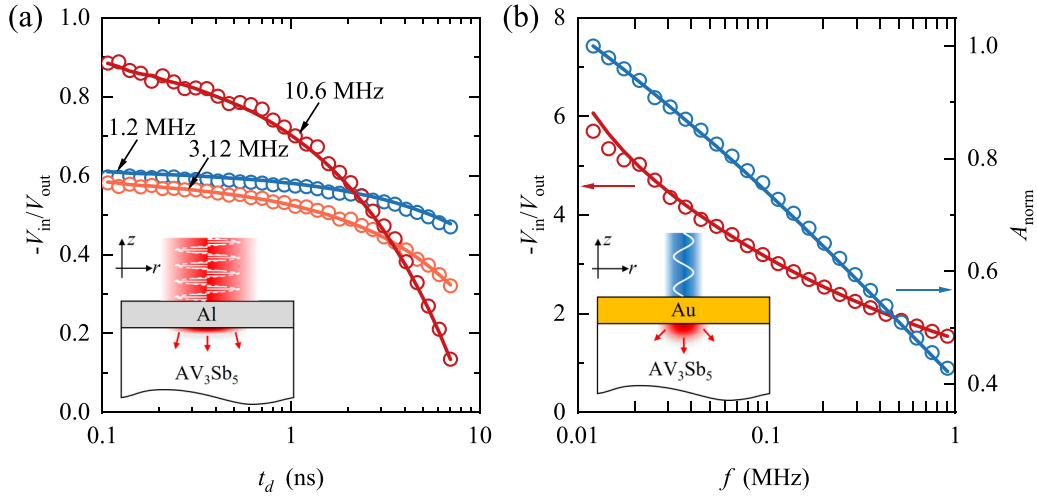

FIG. 2. Experimental (open symbols) the best-fit (solid lines) signals of (a) time-domain thermoreflectance (TDTR) measurements with a root-mean-square spot radius of 20 μm at different modulation frequencies and (b) frequency-domain thermoreflectance (FDTR) measurements (normalized amplitude $A_{\text{norm}} = A(f)/A(0.01\ \text{MHz})$, with $A = \sqrt{V_{\text{in}}^2 + V_{\text{out}}^2}$), measured upon the CsV_3Sb_5 sample. Insets are schematics of thermoreflectance techniques for measuring the anisotropic thermal conductivity.

D8 Venture; the FWHMs are in the range of 0.30–0.35°, indicating that the cross-plane mosaicity of our sample is comparable with the reported literature [41]. The morphology of the synthesized samples is characterized by scanning electron and optical microscopes, and the flat and smooth regions on the sample surface are much larger than the laser spots (∼20 μm in radius), which enabled pump-probe characterizations of thermal conductivity. Energy dispersive x-ray spectroscopy suggests a nice agreement of stochiometric ratio with nominal compositions (A : V : Sb = 1:3:5), and detailed characterization results are included in the Supplemental Material [42] (see also Refs. [43,44] therein). Note that all samples have been exfoliated to expose fresh surfaces using scotch tape before characterizations.

We deposit a 109 nm Al transducer by e-beam physical vapor deposition for time-domain thermoreflectance (TDTR) measurements and a 100 nm Au transducer for frequency-domain thermoreflectance (FDTR) measurements, with the thicknesses measured by the DektakXT profilometer (Bruker, USA). The room-temperature electric conductivities of the transducers are measured as $20.5\ \text{m}\Omega^{-1}\,\text{m}^{-1}$ for Al and $30.1\ \text{m}\Omega^{-1}\,\text{m}^{-1}$ for Au using the four-point probe method. Thermal conductivities of transducers as necessary inputs for pump-probe measurements are then determined as $150\ \text{W}\,\text{m}^{-1}\,\text{K}^{-1}$ for Al and $220\ \text{W}\,\text{m}^{-1}\,\text{K}^{-1}$ using the Wiedemann-Franz law.

B. Pump-probe thermal characterizations

TDTR [36] and FDTR techniques [37] are used to measure the cross-plane and in-plane thermal conductivity (κ_z and κ_r) of AV_3Sb_5, respectively. The implementation of our TDTR and FDTR systems are detailed in Refs. [45–48]. In these pump-probe thermoreflectance measurements, the detected signal contains an in-phase component V_{in} proportional to the instantaneous surface temperature rise in phase with the modulated heating and an out-of-phase component V_{out} due to the heat dissipation in the sample. The ratio signal $-V_{\text{in}}/V_{\text{out}}$ is primarily used to extract thermal properties, such that the proportionality coefficients correlating the absolute magnitude of the detected signal with the surface temperature rise can be normalized. Typical TDTR and FDTR signals are shown in Figs. 2(a) and 2(b), and we discuss the method of separately determining the thermal conductivities along different crystalline directions.

There are three unknown parameters to be determined from pump-probe thermoreflectance measurements, including the in-plane thermal conductivity κ_r, the cross-plane thermal conductivity κ_z, and the interface conductance G between the AV_3Sb_5 substrate and the transducer. To separately determine these parameters, we first performed TDTR measurements; the root-mean-square spot radius is set as 20 μm to ensure that the ratio signal is dominantly sensitive to κ_z. We quantify the sensitivity as the logarithmic derivative of the signal y to the parameter x, $S_x^y = \partial \ln y/\partial \ln x$, as shown in Fig. 3(a), suggesting that the ratio signal is only sensitive to κ_z and is marginally affected by both in-plane thermal conductivity κ_r and interface conductance G between the transducer and the sample. To ensure there is no frequency dependence in cross-plane thermal conductivity, we performed TDTR measurements at different modulation frequencies, and we found that a single set of $\kappa_z = 0.49\ \text{W}\,\text{m}^{-1}\,\text{K}^{-1}$ and $G = 60\ \text{MW}\text{m}^{-2}\,\text{K}^{-1}$ can simultaneously achieve the best fit of the TDTR signals of the CsV_3Sb_5 sample at different modulation frequencies [Fig. 2(a)], indicating that there exists no modulation frequency-dependent thermal transport originated from quasiballistic or nonequilibrium phonons [49].

After κ_z is determined by TDTR measurements, κ_r is measured using the FDTR technique with a tightly focused spot radius of 3 μm and a modulation frequency range $f = 0.01 - 1\text{MHz}$. As shown in Fig. 3(b), the FDTR sensitivity to κ_r is much higher than the other two unknown parameters κ_z and G. The in-plane thermal conductivity κ_r is determined as $8.8 \pm 1.5\ \text{W}\,\text{m}^{-1}\,\text{K}^{-1}$ from the frequency-dependent ratio $-V_{\text{in}}/V_{\text{out}}$. We also cross-checked that the same κ_r obtained by best-fitting the ratio can also reproduce the frequency-dependent amplitude signal [Fig. 2(b)]. Similarly,

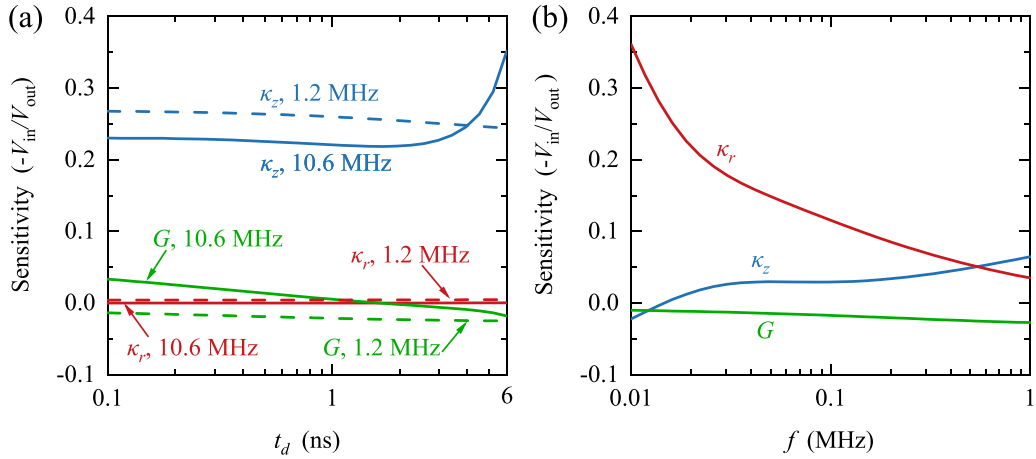

FIG. 3. Sensitivities of (a) time-domain thermoreflectance (TDTR) and (b) frequency-domain thermoreflectance (FDTR) ratio signal to different parameters. The root-mean-square radii are 20 and 3 μm for TDTR and FDTR sensitivity analysis, respectively.

κ_z and κ_r of RbV_3Sb_5 at room temperature are measured as 0.72 ± 0.10 and $12 \pm 2\,\mathrm{W\,m^{-1}\,K^{-1}}$, respectively. Our measurements of κ_r values are consistent with the recent measurements [12,35].

The room-temperature κ_z and κ_r of CsV_3Sb_5 and RbV_3Sb_5 with other typical van der Waals layered materials in Fig. 4(a), and the cross-plane thermal conductivities are not only smaller than glass ($\sim$1.4 $\mathrm{W\,m^{-1}\,K^{-1}}$) [58] but also lower than other van der Waals materials with weak interlayer coupling. As shown in Fig. 4(b), the ultralow κ_z of AV_3Sb_5 is consistent with the reported low group velocity of longitudinal acoustic (LA) phonons (2200 $\mathrm{m\,s^{-1}}$ for RbV_3Sb_5 and 1960 $\mathrm{m\,s^{-1}}$ for CsV_3Sb_5 [20]), indicating weak interlayer coupling strength and soft LA phonons of AV_3Sb_5 are responsible for the low κ_z.

The temperature-dependent TDTR measurements are performed using the Janis VPF 800 cryostat. To avoid large temperature rises at low temperatures beyond the linear thermoreflectance regime, we carefully control the power of the pump and probe beams $<$15 mW, which corresponds to a steady-state temperature rise of $<$10 K. Temperature-dependent thermal conductivities of quartz fused silica and sapphire as standard reference samples are first measured (see Supplemental Material [42]) with excellent agreement with reported literature [39,59]. We also carefully checked the spot-size dependence of the measured thermal conductivity and found that a root-mean-square radius of 20 μm is large enough to avoid any ballistic effects, which could lead to underestimated thermal conductivities [60].

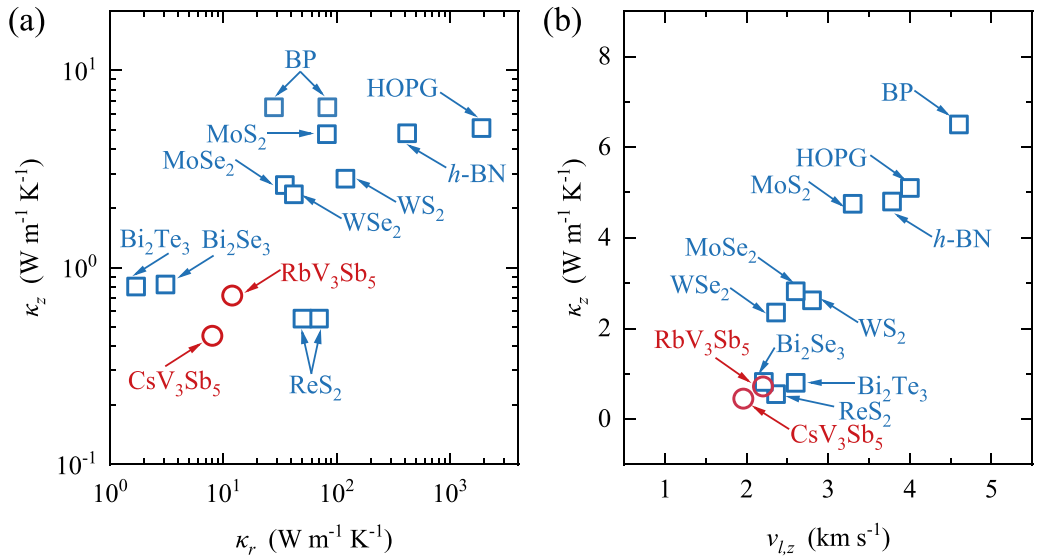

FIG. 4. (a) Summary of experimentally measured cross-plane thermal conductivity κ_z and in-plane thermal conductivity κ_r of layered van der Waals materials at room temperature [45,49,50–53]. (b) Cross-plane thermal conductivity κ_z and longitudinal acoustic (LA) velocity $v_{l,z}$ of AV_3Sb_5 and typical van der Waals layered materials [20,51–57], with BP denoting black phosphorous and HOPG denoting highly ordered pyrolytic graphite.

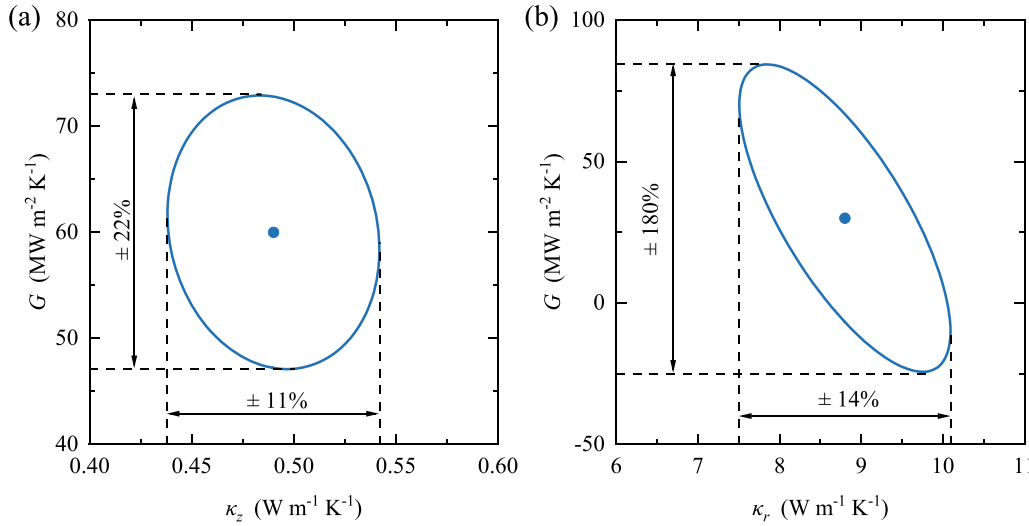

FIG. 5. Confidence intervals (95% confidence level) of thermal transport properties of (a) time-domain thermoreflectance (TDTR) measurement of Al-coated CsV_3Sb_5 sample and (b) frequency-domain thermoreflectance (FDTR) measurement of Au-coated CsV_3Sb_5 sample.

C. Uncertainty analysis

We use the multivariate error propagation formula based on Jacobi matrices for uncertainty analysis [61,62]. The covariance matrix of the unknown parameter vector $\mathbf{X}_U$ is calculated as

$$\mathrm{Var}[\boldsymbol{X}_U] = \left(\boldsymbol{J}_U^T \boldsymbol{J}_U\right)^{-1} \boldsymbol{J}_U^T \left(\mathrm{Var}[\mathbf{y}] + \boldsymbol{J}_P \mathrm{Var}[\boldsymbol{X}_P] \boldsymbol{J}_P^T\right) \boldsymbol{J}_U \left(\boldsymbol{J}_U^T \boldsymbol{J}_U\right)^{-1}, \tag{1}$$

where the superscript T represents the matrix transpose, $\mathbf{J}_U = \partial \mathbf{R}/\partial \mathbf{X}_U$ and $\mathbf{J}_P = \partial \mathbf{R}/\partial \mathbf{X}_P$ are the Jacobian matrices correlating the ratio signal $\mathbf{R}$ (array of ratio values depending on delay time in TDTR or modulation frequency in FDTR) and the unknown parameters $\mathbf{X}_U$ or control parameters $\mathbf{X}_P$, respectively. In this paper, the control parameters $\mathbf{X}_P$ include the root-mean-square radius w, thickness and thermal properties of the metal transducers, and the heat capacity of AV_3Sb_5. Typical uncertainty levels are 10% for κ of Al or Au transducers, 3% for C of the transducers and AV_3Sb_5 samples, 4% for the transducer thickness, and 5% for the root-mean-square spot radius. For TDTR measurements, the vector of unknown parameter $\mathbf{X}_U$ includes κ_z of AV_3Sb_5 and the interface conductance G. After TDTR measurements are performed, κ_z is included as the control parameter $\mathbf{X}_P$ when performing uncertainty analysis of FDTR, and $\mathbf{X}_U$ of FDTR only includes κ_r and G. An example of the $\mathrm{Var}[\mathbf{X}_U]$ for TDTR and FDTR fitting of CsV_3Sb_5 at 300 K can be seen in the Supplemental Material [42], and the uncertainties $2(\sigma)$ of each unknown parameter can be calculated as the square root of the diagonal elements of the matrix $\mathrm{Var}[\mathbf{X}_U]$. Using the covariance matrix $\mathrm{Var}[\mathbf{X}_U]$, the multivariate confidence interval is determined as ellipsoid [45], as shown in Fig. 5.

D. Resistivity and thermal conductivity of electrons

Figure. 6(a) shows the temperature-dependent resistivity ρ_r of AV_3Sb_5 along the in-plane direction, measured using a physical property measurement system, and the estimated electron in-plane thermal conductivity $\kappa_{r,e}$ using the Wiedemann-Franz law is shown in Fig. 6(b). Inflection points in both ρ_r and $\kappa_{r,e}$ are observed at 102 K for RbV_3Sb_5 RbV_3Sb_5 and 94 K for CsV_3Sb_5, agreeing well with the reported T_{CDW} in previous literature [8,19].

Due to the small thicknesses (50–90 μm) of our samples, it is challenging to directly measure the cross-plane resistivity and the electronic contribution to the cross-plane thermal conductivity $\kappa_{z,e}$. However, we estimate that electrons contribute negligibly to $\kappa_{z,e}$. Due to the unique layered structure and weak interlayer coupling strengths, the Fermi surface of AV_3Sb_5 has been reported to show strong 2D features [18], resulting in a high anisotropy ratio $\rho_z/\rho_r \sim 600$ from 2 to 300 K characterized by Ortiz *et al.* [8] Therefore, we expect the electronic cross-plane thermal conductivity $\kappa_{z,e}$ is on the order of $\sim$0.01 $\mathrm{W\,m^{-1}\,K^{-1}}$ at 300 K, which is negligibly small compared with the measured κ_z of CsV_3Sb_5 (0.49 $\mathrm{W\,m^{-1}\,K^{-1}}$) and RbV_3Sb_5 (0.72 $\mathrm{W\,m^{-1}\,K^{-1}}$).

III. HOPPINGLIKE CROSS-PLANE THERMAL TRANSPORT

The temperature-dependent κ_z (40–500 K) of RbV_3Sb_5 and CsV_3Sb_5 is shown in Figs. 7(a) and 7(b). Interestingly, the cross-plane thermal conductivity κ_z shows a glasslike temperature dependence with thermal conductivity decreasing monotonically as the temperature decreases. The thermal conductivity even drops below the Cahill-Pohl limit [39] at temperatures lower than T_{CDW}. The Cahill-Pohl limit can be regarded as the minimum thermal conductivity of the quasiparticle transport regime by assuming that the mean free paths of all phonons are equal to half of the wavelengths. Since RbV_3Sb_5 and CsV_3Sb_5 are anisotropic layered materials, we also compare the measured κ_z with the extended anisotropic Cahill-Pohl model proposed by Chen and Dames [63] which included effects of phonon focusing and first Brillouin zone truncation. The fact that κ_z drops below both the isotropic and anisotropic Cahill-Pohl model suggests possible existence of

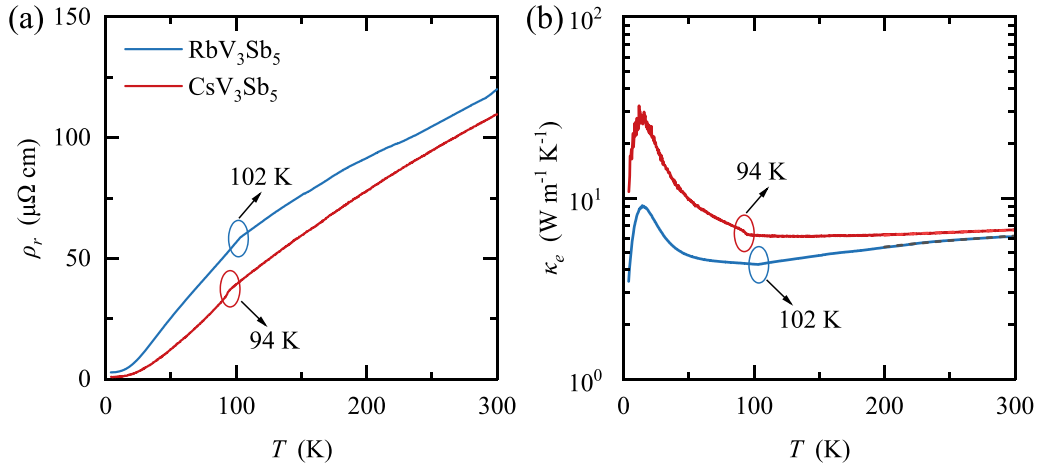

FIG. 6. (a) In-plane resistivity and (b) in-plane electron thermal conductivity of AV_3Sb_5 (A = Rb, Cs).

localized phonons [65], which is consistent with the recent observation of nearly flat phonon branches in AV_3Sb_5 [28].

Considering these localized modes could be well described by Einstein oscillators, we proposed a hopping model to describe the cross-plane thermal transport [65]. In general, the lattice thermal conductivity of crystalline solids can be expressed as a frequency-dependent integral over the phonon spectrum:

$$\kappa_{\rm ph}(T) = \int C(\omega)D(\omega)d\omega, \tag{2}$$

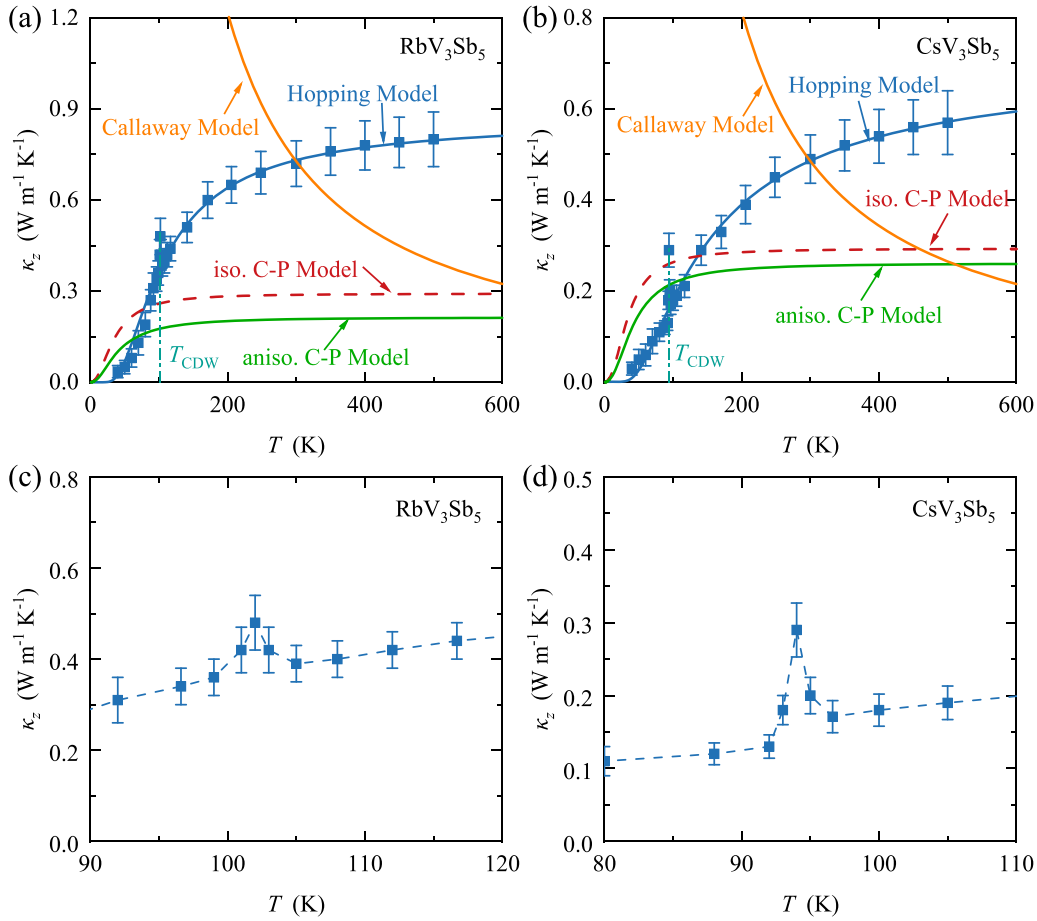

FIG. 7. Measured cross-plane thermal conductivity κ_z of (a) RbV_3Sb_5 and (b) CsV_3Sb_5 over the temperature range of 40–500 K, compared with the proposed hopping model, isotropic Cahill-Pohl (iso. C-P) model [39], anisotropic Cahill-Pohl (aniso. C-P) model [63] and Callaway model [64]. Details for the peak in κ_z around $T_{\rm CDW}$ for (c) RbV_3Sb_5 and (d) CsV_3Sb_5.

where $C(\omega) = \hbar\omega g(\omega)\frac{\partial f}{\partial T}$ is the spectral volumetric specific heat, with f the Bose-Einstein distribution and $g(\omega)$ the density of states, and $D(\omega)$ is spectral diffusivity. In this paper, our hopping model separately treats the propagating low-frequency phonons and the high-frequency localized modes. The propagating low-frequency phonons is described by the Callaway model [64], while localized high-frequency modes are treated as Einstein oscillators. Therefore, the vibrational density of states is written as

$$g(\omega) = \begin{cases} 3\omega^2/\left(2\pi^2 v_s^3\right), & \omega < \omega_c \\ 3n_E\delta(\omega - \omega_E), & \omega > \omega_c \end{cases}, \tag{3}$$

where ω_c is the cutoff frequency between the propagating phonons and localized modes, v_s is the averaged acoustic velocity, and n_E denotes the number density of Einstein oscillators. With the Debye approximation, the total number of propagating modes below ω_c should be equal to $3(n - n_E)$, therefore:

$$\int_0^{\omega_c} g(\omega)d\omega = 3(n - n_E). \tag{4}$$

We can then derive an explicit expression correlating n_E and ω_c:

$$\omega_c = \left[6\pi^2 v_s^3 (n - n_E)\right]^{1/2}, \tag{5}$$

where n is the number density of atoms. Following Allen and Feldman's [66] definition of spectral thermal diffusivity $D(\omega)$, the thermal conductivity can be computed by integrating $C(\omega)D(\omega)$ over the vibrational spectrum. For low-frequency propagating phonons, $D(\omega)$ is simply $v(\omega)^2\tau(\omega)/3$ from the phonon-gas model, with $\tau(\omega)$ denoting the relaxation time. The dynamics of the localized modes can be described by a random walk theory [67], where $D(\omega)$ is determined by hopping length α, with the hopping rates expressed as ω/π [68], and probability of a successful hopping denoted as P. Considering the structural fluctuation at finite temperatures, we phenomenologically describe the probability of successful hopping P using the Arrhenius law $P = A\exp(-E_a/k_BT)$, where E_a is activation energy and A is the preexponential factor. Therefore, $D(\omega)$ over the phonon spectrum is expressed as

$$D(\omega) = \begin{cases} \frac{1}{3}v_s^2\tau(\omega), & \omega < \omega_c \\ \alpha^2\frac{\pi}{\omega}A\exp\left(-\frac{E_a}{k_BT}\right), & \omega > \omega_c \end{cases}. \tag{6}$$

Integrating over the vibrational spectra, the lattice thermal conductivity based on the hopping model is written as

$$\kappa_{\rm ph}(T) = k_B(n - n_E)\sum_j v_j^2\left(\frac{T}{\theta_{cj}}\right)^3\int_0^{\frac{\theta_{cj}}{T}}\frac{x^4 e^x}{(e^x - 1)^2}\tau(x, T)dx + 3n_E k_B\frac{x_E^2 e^x}{(e^{x_E} - 1)^2}\frac{\alpha^2\pi}{\omega_E}P(T), \tag{7}$$

where $x = \frac{\hbar\omega}{k_BT}$, k_B is Boltzmann constant, $\tau(x, T)$ is spectral relaxation time, and v_j is the group velocity of acoustic branch j. Here, θ_{cj} is like the Debye temperature of branch j, defined as $\theta_{cj} = \hbar\omega_{cj}/k_B$. Also, ω_E denotes the average frequency of Einstein oscillators. More details of the hopping model are included in the Supplemental Material. Figures 7(a) and 7(b) show that the hopping model captures the glasslike $\kappa_z(T)$. Our measurement also observed a peak [Figs. 7(c) and 7(d)] at $T_{\rm CDW}$ in temperature-dependent κ_z, which is consistent with recent observations of lattice distortions in the cross-plane direction [17,18].

IV. CONCLUSIONS

In summary, we report on the temperature-dependent thermal conductivity of the kagome metals AV_3Sb_5 (A = Rb, Cs) using pump-probe thermoreflectance techniques. At room temperature, the cross-plane thermal conductivities are determined as 0.72 and 0.49 $\mathrm{W\,m^{-1}\,K^{-1}}$ for RbV_3Sb_5 and CsV_3Sb_5, respectively. The low κ_z arises from strongly suppressed phonon group velocity associated with weak interlayer bonding. Unique glasslike temperature dependence of κ_z is observed, with the cross-plane thermal conductivity dropping monotonically even below the Cahill-Pohl limit as the temperature decreases lower than $T_{\rm CDW}$. The glasslike κ_z can be well captured by a hopping transport picture of localized phonon. Sudden increase in κ_z is also experimentally observed at $T_{\rm CDW}$, supporting recent identifications of 3D CDW transitions where the lattice distortions are modulated in the cross-plane direction.

ACKNOWLEDGMENTS

X.Q. acknowledges support from China's National Key R&D Project (Grant No. 2022YFA1203100). R.Y. thanks the support from the National Natural Science Foundation of China (NSFC Grant No. 52276065). Z.W. acknowledges support from the National Natural Science Foundation of China (Grant No. 92065109), and the Beijing Natural Science Foundation (Grants No. Z190006 and No. Z210006). J.Z. is grateful for support from the National Natural Science Foundation of China (NSFC Grant No. 51976025). Y.P. acknowledges the support from Cross-Discipline Ph.D. Education Plan by HUST. Z.W. thanks the Analysis & Testing Center at BIT for assistance and support.

The authors declare no conflict of interest.

Author contributions: X.Q., R.Y., and Z.W. conceptualized this work; Y.P., H.Y., X.F., and J.Z. performed pump-probe measurements; X.Q. and Y.P. analyzed the data and conducted theoretical analysis; J.L., Z.W., and Y.Y. synthesized and characterized the samples; Y.P., X.Q., and R.Y. wrote the manuscript, X.Q. and R.Y. supervised this work. All authors discussed and edited the manuscript.

[1] L. Ye, M. Kang, J. Liu, F. von Cube, C. R. Wicker, T. Suzuki, C. Jozwiak, A. Bostwick, E. Rotenberg, D. C. Bell *et al.*, Massive dirac fermions in a ferromagnetic kagome metal, Nature (London) **555**, 638 (2018).

[2] M. Kang, L. Ye, S. Fang, J.-S. You, A. Levitan, M. Han, J. I. Facio, C. Jozwiak, A. Bostwick, E. Rotenberg *et al.*, Dirac fermions and flat bands in the ideal kagome metal FeSn, Nat. Mater. **19**, 163 (2020).

[3] S. Yan, D. A. Huse, and S. R. White, Spin-liquid ground state of the $S = \frac{1}{2}$ kagome heisenberg antiferromagnet, Science **332**, 1173 (2011).

[4] S. V. Isakov, S. Wessel, R. G. Melko, K. Sengupta, and Y. B. Kim, Hard-core bosons on the kagome lattice: Valence-bond solids and their quantum melting, Phys. Rev. Lett. **97**, 147202 (2006).

[5] W.-H. Ko, P. A. Lee, and X.-G. Wen, Doped kagome system as exotic superconductor, Phys. Rev. B **79**, 214502 (2009).

[6] H.-M. Guo and M. Franz, Topological insulator on the kagome lattice, Phys. Rev. B **80**, 113102 (2009).

[7] B. R. Ortiz, L. C. Gomes, J. R. Morey, M. Winiarski, M. Bordelon, J. S. Mangum, I. W. H. Oswald, J. A. Rodriguez-Rivera, J. R. Neilson, S. D. Wilson *et al.*, New kagome prototype materials: Discovery of KV_3Sb_5, RbV_3Sb_5, and CsV_3Sb_5, Phys. Rev. Mater. **3**, 094407 (2019).

[8] B. R. Ortiz, S. M. L. Teicher, Y. Hu, J. L. Zuo, P. M. Sarte, E. C. Schueller, A. M. M. Abeykoon, M. J. Krogstad, S. Rosenkranz *et al.*, CsV_3Sb_5: A $\mathbb{Z}_2$ topological kagome metal with a superconducting ground state, Phys. Rev. Lett. **125**, 247002 (2020).

[9] B. R. Ortiz, P. M. Sarte, E. M. Kenney, M. J. Graf, S. M. L. Teicher, R. Seshadri, and S. D. Wilson, Superconductivity in the $\mathbb{Z}_2$ kagome metal KV_3Sb_5, Phys. Rev. Mater. **5**, 034801 (2021).

[10] H. Zhao, H. Li, B. R. Ortiz, S. M. L. Teicher, T. Park, M. Ye, Z. Wang, L. Balents, S. D. Wilson, and I. Zeljkovic, Cascade of correlated electron states in the kagome superconductor CsV_3Sb_5, Nature (London) **599**, 216 (2021).

[11] Y. Fu, N. Zhao, Z. Chen, Q. Yin, Z. Tu, C. Gong, C. Xi, X. Zhu, Y. Sun, K. Liu *et al.*, Quantum transport evidence of topological band structures of kagome superconductor CsV_3Sb_5, Phys. Rev. Lett. **127**, 207002 (2021).

[12] X. Zhou, H. Liu, W. Wu, K. Jiang, Y. Shi, Z. Li, Y. Sui, J. Hu, and J. Luo, Anomalous thermal Hall effect and anomalous nernst effect of CsV_3Sb_5, Phys. Rev. B **105**, 205104 (2022).

[13] H. Li, H. Zhao, B. R. Ortiz, T. Park, M. Ye, L. Balents, Z. Wang, S. D. Wilson, and I. Zeljkovic, Rotation symmetry breaking in the normal state of a kagome superconductor KV_3Sb_5, Nat. Phys. **18**, 265 (2022).

[14] M. Kang, S. Fang, J. Yoo, B. R. Ortiz, Y. M. Oey, J. Choi, S. H. Ryu, J. Kim, C. Jozwiak, A. Bostwick *et al.*, Charge order landscape and competition with superconductivity in kagome metals, Nat. Mater. **22**, 186 (2023).

[15] Y. Li, Q. Li, X. Fan, J. Liu, Q. Feng, M. Liu, C. Wang, J.-X. Yin, J. Duan, X. Li *et al.*, Tuning the competition between superconductivity and charge order in the kagome superconductor $Cs(V_{1-x}Nb_x)_3Sb_5$, Phys. Rev. B **105**, L180507 (2022).

[16] T. Kato, Y. Li, K. Nakayama, Z. Wang, S. Souma, F. Matsui, M. Kitamura, K. Horiba, H. Kumigashira, T. Takahashi *et al.*, Fermiology and origin of T_c enhancement in a kagome superconductor $Cs(V_{1-x}Nb_x)_3Sb_5$, Phys. Rev. Lett. **129**, 206402 (2022).

[17] Z. Liang, X. Hou, F. Zhang, W. Ma, P. Wu, Z. Zhang, F. Yu, J.-J. Ying, K. Jiang, L. Shan *et al.*, Three-dimensional charge density wave and surface-dependent vortex-core states in a kagome superconductor CsV_3Sb_5, Phys. Rev. X **11**, 031026 (2021).

[18] B. R. Ortiz, S. M. L. Teicher, L. Kautzsch, P. M. Sarte, N. Ratcliff, J. Harter, J. P. C. Ruff, R. Seshadri, and S. D. Wilson, Fermi surface mapping and the nature of charge-density-wave order in the kagome superconductor CsV_3Sb_5, Phys. Rev. X **11**, 041030 (2021).

[19] Q. Yin, Z. Tu, C. Gong, Y. Fu, S. Yan, and H. Lei, Superconductivity and normal-state properties of kagome metal RbV_3Sb_5 single crystals, Chin. Phys. Lett. **38**, 037403 (2021).

[20] H. Tan, Y. Liu, Z. Wang, and B. Yan, Charge density waves and electronic properties of superconducting kagome metals, Phys. Rev. Lett. **127**, 046401 (2021).

[21] H. Chen, H. Yang, B. Hu, Z. Zhao, J. Yuan, Y. Xing, G. Qian, Z. Huang, G. Li, Y. Ye *et al.*, Roton pair density wave in a strong-coupling kagome superconductor, Nature (London) **599**, 222 (2021).

[22] N. Shumiya, Md. S. Hossain, J.-X. Yin, Y.-X. Jiang, B. R. Ortiz, H. Liu, Y. Shi, Q. Yin, H. Lei, S. S. Zhang *et al.*, Intrinsic nature of chiral charge order in the kagome superconductor RbV_3Sb_5, Phys. Rev. B **104**, 035131 (2021).

[23] Y.-X. Jiang, J.-X. Yin, M. M. Denner, N. Shumiya, B. R. Ortiz, G. Xu, Z. Guguchia, J. He, M. S. Hossain, X. Liu *et al.*, Unconventional chiral charge order in kagome superconductor KV_3Sb_5, Nat. Mater. **20**, 1353 (2021).

[24] H. Li, T. T. Zhang, T. Yilmaz, Y. Y. Pai, C. E. Marvinney, A. Said, Q. W. Yin, C. S. Gong, Z. J. Tu, E. Vescovo *et al.*, Observation of unconventional charge density wave without acoustic phonon anomaly in kagome superconductors AV_3Sb_5 (A = Rb, Cs), Phys. Rev. X **11**, 031050 (2021).

[25] C. Li, X. Wu, H. Liu, C. Polley, Q. Guo, Y. Wang, X. Han, M. Dendzik, M. H. Berntsen, B. Thiagarajan *et al.*, Coexistence of two intertwined charge density waves in a kagome system, Phys. Rev. Res. **4**, 033072 (2022).

[26] Q. Xiao, Y. Lin, Q. Li, X. Zheng, S. Francoual, C. Plueckthun, W. Xia, Q. Qiu, S. Zhang, Y. Guo *et al.*, Coexistence of multiple stacking charge density waves in kagome superconductor CsV_3Sb_5, Phys. Rev. Res. **5**, L012032 (2023).

[27] L. Kautzsch, B. R. Ortiz, K. Mallayya, J. Plumb, G. Pokharel, J. P. C. Ruff, Z. Islam, E.-A. Kim, R. Seshadri, and S. D. Wilson, Structural evolution of the kagome superconductors AV_3Sb_5 (A = K, Rb, and Cs) through charge density wave order, Phys. Rev. Mater. **7**, 024806 (2023).

[28] D. Subires, A. Korshunov, A. H. Said, L. Sánchez, B. R. Ortiz, S. D. Wilson, A. Bosak, and S. Blanco-Canosa, Order-disorder charge density wave instability in the kagome metal (Cs, Rb)V_3Sb_5, Nat. Commun. **14**, 1015 (2023).

[29] R. S. Kwok and S. E. Brown, Thermal conductivity of the charge-density-wave systems $K_{0.3}MoO_3$ and $(TaSe_4)_2I$ near the Peierls transition, Phys. Rev. Lett. **63**, 895 (1989).

[30] P. A. Lee, T. M. Rice, and P. W. Anderson, Conductivity from charge or spin density waves, Solid State Commun. **14**, 703 (1997).

[31] M. D. Núñez-Regueiro, J. M. Lopez-Castillo, and C. Ayache, Thermal conductivity of $1T-TaS_2$ and $2H-TaSe_2$, Phys. Rev. Lett. **55**, 1931 (1985).

[32] H. Liu, C. Yang, B. Wei, L. Jin, A. Alatas, A. Said, S. Tongay, F. Yang, A. Javey, J. Hong *et al.*, Anomalously suppressed thermal conduction by electron-phonon coupling in charge-density-wave tantalum disulfide, Adv. Sci. **7**, 1902071 (2020).

[33] S. Gerber, H. Jang, H. Nojiri, S. Matsuzawa, H. Yasumura, D. A. Bonn, R. Liang, W. N. Hardy, Z. Islam, A. Mehta *et al.*, Three-dimensional charge density wave order in $YBa_2Cu_3O_{6.67}$ at high magnetic fields, Science **350**, 949 (2015).

[34] Z. Wang, Q. Yin, S. Yan, L. Wu, X. Wu, M. Li, W. Song, Q. Liu, H. Ma, W. Ji *et al.*, Three-dimensional charge density wave observed by angle-resolved photoemission spectroscopy in $1T-VSe_2$, Phys. Rev. B **104**, 155134 (2021).

[35] K. Yang, W. Xia, X. Mi, L. Zhang, Y. Gan, A. Wang, Y. Chai, X. Zhou, X. Yang, Y. Guo *et al.*, Charge Fluctuations above T_{CDW} revealed by glasslike thermal transport in kagome metals AV_3Sb_5 (A = K, Rb, Cs), Phys. Rev. B **107**, 184506 (2023).

[36] D. G. Cahill, Analysis of heat flow in layered structures for time-domain thermoreflectance, Rev. Sci. Instrum. **75**, 5119 (2004).

[37] A. J. Schmidt, R. Cheaito, and M. Chiesa, A frequency-domain thermoreflectance method for the characterization of thermal properties, Rev. Sci. Instrum. **80**, 094901 (2009).

[38] P. Jiang, X. Qian, and R. Yang, Tutorial: Time-domain thermoreflectance (TDTR) for thermal property characterization of bulk and thin film materials, J. Appl. Phys. **124**, 161103 (2018).

[39] D. G. Cahill, S. K. Watson, and R. O. Pohl, Lower limit to the thermal conductivity of disordered crystals, Phys. Rev. B **46**, 6131 (1992).

[40] Z. Wang, Y.-X. Jiang, J.-X. Yin, Y. Li, G.-Y. Wang, H.-L. Huang, S. Shao, J. Liu, P. Zhu, N. Shumiya *et al.*, Electronic nature of chiral charge order in the kagome superconductor CsV_3Sb_5, Phys. Rev. B **104**, 075148 (2021).

[41] S. Ni, S. Ma, Y. Zhang, J. Yuan, H. Yang, Z. Lu, N. Wang, J. Sun, Z. Zhao, D. Li *et al.*, Anisotropic superconducting properties of kagome metal CsV_3Sb_5, Chin. Phys. Lett. **38**, 057403 (2021).

[42] See Supplemental Material at http://link.aps.org/supplemental/10.1103/PhysRevB.108.205112 for more information about sensitivity analysis, uncertainty analysis, the temperature-dependent experiment, and the hopping model. It also contains Refs. [43,44].

[43] H. T. Smyth, H. S. Skogen, and W. B. Harsell, Thermal capacity of vitreous silica, J. Am. Ceram. Soc. **36**, 327 (1953).

[44] D. A. Ditmars, S. Ishihara, S. S. Chang, G. Bernstein, and E. D. West, Enthalpy and heat-capacity standard reference material: Synthetic sapphire ($\alpha-Al_2O_3$) From 10 to 2250 K, J. Res. Natl. Bur. Stan. **87**, 159 (1982).

[45] X. Qian, Z. Ding, J. Shin, A. J. Schmidt, and G. Chen, Accurate measurement of in-plane thermal conductivity of layered materials without metal film transducer using frequency domain thermoreflectance, Rev. Sci. Instrum. **91**, 064903 (2020).

[46] Y. Pang, P. Jiang, and R. Yang, Machine learning-based data processing technique for time-domain thermoreflectance (TDTR) measurements, J. Appl. Phys. **130**, 084901 (2021).

[47] P. Jiang, D. Wang, Z. Xiang, R. Yang, and H. Ban, A new spatial-domain thermoreflectance method to measure a broad range of anisotropic in-plane thermal conductivity, Int. J. Heat Mass Transf. **191**, 122849 (2022).

[48] Y. Pang, Y. Li, Z. Gao, X. Qian, X. Wang, J. Hong, and P. Jiang, Thermal transport manipulated by vortex domain walls in bulk $h-ErMnO_3$, Mater. Today Phys. **31**, 100972 (2023).

[49] P. Jiang, X. Qian, X. Gu, and R. Yang, Probing anisotropic thermal conductivity of transition metal dichalcogenides MX_2 (M = Mo, W and X = S, Se) using time-domain thermoreflectance, Adv. Mater. **29**, 1701068 (2017).

[50] K. H. Park, M. Mohamed, Z. Aksamija, and U. Ravaioli, Phonon scattering due to van der waals forces in the lattice thermal conductivity of Bi_2Te_3 thin films, J. Appl. Phys. **117**, 015103 (2015).

[51] B. Sun, X. Gu, Q. Zeng, X. Huang, Y. Yan, Z. Liu, R. Yang, and Y. K. Koh, Temperature dependence of anisotropic thermal-conductivity tensor of bulk black phosphorus, Adv. Mater. **29**, 1603297 (2017).

[52] P. Jiang, X. Qian, R. Yang, and L. Lindsay, Anisotropic thermal transport in bulk hexagonal boron nitride, Phys. Rev. Mater. **2**, 064005 (2018).

[53] H. Jang, C. R. Ryder, J. D. Wood, M. C. Hersam, and D. G. Cahill, 3*d* anisotropic thermal conductivity of exfoliated rhenium disulfide, Adv. Mater. **29**, 1700650 (2017).

[54] D. O. Lindroth and P. Erhart, Thermal transport in van der Waals solids from first-principles calculations, Phys. Rev. B **94**, 115205 (2016).

[55] R. Guo, P. Jiang, T. Tu, S. Lee, B. Sun, H. Peng, and R. Yang, Electrostatic interaction determines thermal conductivity anisotropy of Bi_2O_2Se, Cell Rep. Phys. Sci. **2**, 100624 (2021).

[56] Y. Wang, C. Liebig, X. Xu, and R. Venkatasubramanian, Acoustic phonon scattering in Bi_2Te_3/Sb_2Te_3 superlattices, Appl. Phys. Lett. **97**, 083103 (2010).

[57] M. Mohr, J. Maultzsch, E. Dobardžić, S. Reich, I. Milošević, M. Damnjanović, A. Bosak, M. Krisch, and C. Thomsen, Phonon dispersion of graphite by inelastic x-ray scattering, Phys. Rev. B **76**, 035439 (2007).

[58] X. Qian and R. Yang, Machine learning for predicting thermal transport properties of solids, Mater. Sci. Eng. R: Rep. **146**, 100642 (2021).

[59] D. G. Cahill, S.-M. Lee, and T. I. Selinder, Thermal conductivity of $\kappa-Al_2O_3$ and $\alpha-Al_2O_3$ wear-resistant coatings, J. Appl. Phys. **83**, 5783 (1998).

[60] R. B. Wilson and D. G. Cahill, Anisotropic failure of fourier theory in time-domain thermoreflectance experiments, Nat. Commun. **5**, 5075 (2014).

[61] J. Yang, E. Ziade, and A. J. Schmidt, Uncertainty analysis of thermoreflectance measurements, Rev. Sci. Instrum. **87**, 014901 (2016).

[62] X. Qian, P. Jiang, and R. Yang, Anisotropic thermal conductivity of 4*h* and 6*h* silicon carbide measured using time-domain thermoreflectance, Mater. Today Phys. **3**, 70 (2017).

[63] Z. Chen and C. Dames, An anisotropic model for the minimum thermal conductivity, Appl. Phys. Lett. **107**, 193104 (2015).

[64] J. Callaway, Model for lattice thermal conductivity at low temperatures, Phys. Rev. **113**, 1046 (1959).

[65] Q. Xi, Z. Zhang, J. Chen, J. Zhou, T. Nakayama, and B. Li, Hopping processes explain linear rise in temperature of thermal conductivity in thermoelectric clathrates with off-center guest atoms, Phys. Rev. B **96**, 064306 (2017).

[66] P. B. Allen and J. L. Feldman, Thermal conductivity of disordered harmonic solids, Phys. Rev. B **48**, 12581 (1993).

[67] M. T. Agne, R. Hanus, and G. J. Snyder, Minimum thermal conductivity in the context of *diffuson*-mediated thermal transport, Energy Environ. Sci. **11**, 609 (2018).

[68] A. Einstein, Elementare Betrachtungen über die thermische Molekularbewegung in festen Körpern, Ann. Phys. **340**, 679 (1911).

Correction: Support statements in the Acknowledgments have been corrected.